THE JOURNAL OF
PHYSICAL CHEMISTRY C

Article

pubs.acs.org/JPCC

Van der Waals Interactions and Anharmonicity in the Lattice Vibrations, Dielectric Constants, Effective Charges, and Infrared Spectra of the Organic−Inorganic Halide Perovskite $CH_3NH_3PbI_3$

Miguel A. Pérez-Osorio,[†] Aurélie Champagne,[‡] Marios Zacharias,[†] Gian-Marco Rignanese,[‡] and Feliciano Giustino*,[†]

[†]Department of Materials, University of Oxford, Parks Road, Oxford OX1 3PH, United Kingdom

[‡]Institute of Condensed Matter and Nanoscience (IMCN), Université catholique de Louvain, B-1348 Louvain-la-neuve, Belgium

ABSTRACT: Using first-principles calculations, we perform a comprehensive and systematic analysis to establish the role of van der Waals (vdW) interactions and anharmonicity in the vibrational properties of the low-temperature orthorhombic phase of the hybrid perovskite $CH_3NH_3PbI_3$. To this end, we consider the most common approaches for including vdW effects in our phonon calculations: the semiempirical Grimme approximations, the Tkatchenko-Scheffler dispersion corrections, and the vdW density-functional method. The vibrational normal modes are first calculated within the harmonic approximation. We consider the LDA and GGA approximations to the exchange-correlation functional and include spin−orbit coupling (SOC) effects. On top of the harmonic calculations, we also evaluate the anharmonicity of the normal modes and the phonon−phonon coupling by solving one-dimensional and two-dimensional nuclear Schrödinger equations, respectively, via the finite-displacement method. We observe that both the LDA and GGA approximations work remarkably well in describing the vibrational properties of $CH_3NH_3PbI_3$. We find that vdW effects and relativistic effects do not have any significant impact on the vibrational properties of $CH_3NH_3PbI_3$. Our study also reveals that the spinning modes of the organic $CH_3NH_3^+$ cations carry considerable anharmonicity but that the anharmonic coupling between different modes is relatively small.

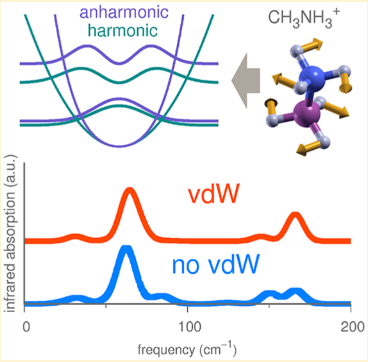

1. INTRODUCTION

The organic−inorganic halide perovskite $MAPbI_3$ (MA = CH_3NH_3) and its related compounds are considered key emerging materials in energy research, owing to their high performance in solution-processable solar cells.[1−11] Other promising applications of this important class of materials include light-emitting diodes and solar-to-fuel energy conversion devices.[12,13] During the past two decades, many efforts have been devoted toward unraveling the origin of the outstanding performance of this perovskite family in photovoltaic devices.[14] It was found that $MAPbI_3$ has unique electronic and optical properties: it has a small direct band gap of 1.6 eV and a high absorption coefficient across the visible spectrum.[3,10] The excitons created upon light absorption have a weak binding energy (20 meV),[15] leading to thermal dissociation of electron−hole pairs. Owing to the low effective masses of the free electron and hole carriers, they can travel through the perovskite matrix with relatively high mobilities (50 cm^{2}V^{-1}s^{-1}).[16,17] In addition, the recombination rates of the charge carriers are relatively low, leading to long carrier diffusion lengths, which enable efficient charge extraction.[13,18,19]

The vibrational properties of $MAPbI_3$ have also been actively investigated, as they are highly relevant for further understanding the optoelectronic properties of this material.[7,16,20−25] Having solid data on the infrared and Raman spectra of $MAPbI_3$ is essential not only because they can be used in the characterization of this perovskite but also because much information on the structural, mechanical, and electronic properties of $MAPbI_3$ can be derived from these spectra, e.g., dielectric properties, heat capacities, charge carrier and relaxations rates, phase transitions, and degradation processes.[9,26,27] First-principles phonon calculations reveal that vibrations of $MAPbI_3$ can be classified as internal vibrations of the organic MA cations (with frequencies ranging between 300 and 3200 cm^{-1}), librations and spinning of these cations (with frequencies between 60 and 180 cm^{-1}), and internal vibrations of the inorganic PbI_3 network (with frequencies below 120 cm^{-1}).[24] A complete description of these normal modes, including their symmetry and character, was recently proposed.[24] In a previous work[24] by some of us, we predicted a large LO-TO splitting in $MAPbI_3$ for the low-frequency B_{3u} Pb−I stretching mode. This LO-TO splitting was recently measured by two independent groups. Wright et al.[19] estimated the frequency of the LO normal mode via temperature-dependent photoluminescence measurements, and soon after, Sender et al.[28] determined the frequency of this normal mode by means of infrared spectroscopy measurements at oblique incidence. Moreover, Wright et al.[19] found that the scattering

Received: July 19, 2017
Published: August 4, 2017

from LO phonons via the Fröhlich interaction is the dominant source of electron−phonon coupling in $MAPbI_3$ and related compounds. This discovery is important for the development of high-efficiency perovskite solar cells, as phonon scattering intrinsically limits the charge-carrier mobilities.

The infrared and Raman spectra of $MAPbI_3$ were measured by several groups.[29−32] The experimental infrared spectra reported in the literature are generally consistent with one another.[24,25,27] On the other hand, one can find substantial differences between the reported Raman spectra.[29,30] The origin of these discrepancies possibly lies in the fact that $MAPbI_3$ can undergo degradation during the Raman measurement due to the laser beam.[30,33,34] Thus, some Raman peaks may not correspond to $MAPbI_3$ but to degradation products, for instance, PbI_2 and MAI as it was found by Ledinsky et al.[29] In the particular case of the infrared spectra of $MAPbI_3$, for most of the measured peaks there is a very good agreement with calculations, except for two peaks with frequencies 155 and 175 cm^{-1}, assigned to librations of the organic MA cations.[24] The frequencies of these two peaks are overestimated in the calculations by ∼100 cm^{-1}. The origin of such an overestimation is currently unclear. In our previous work,[24] using a perturbative approach we found that vdW interactions, described via the semiempirical Grimme approach,[35] slightly red shift the calculated frequencies of the libration modes of the MA cations, reducing the discrepancy by as much as 30%. This is not enough to account for the deviation between theory and experiment; however, it points to the need for an in-depth investigation to clarify whether the vibrational frequencies are affected by vdW effects. Furthermore, this raises the question as to whether the calculated infrared intensities depend on vdW effects. To our knowledge, this possibility has not been investigated yet.

Besides vdW interactions, anharmonicity is another effect that may explain the overestimation of the libration frequencies. As far as we know, anharmonic effects have been investigated only for the soft modes of the high-temperature phase of $MAPbI_3$.[25,36]

In order to ascertain the role of vdW interactions and anharmonicity in the vibrational properties of $MAPbI_3$, we here perform a systematic study of the lattice dynamics. We calculate normal-mode frequencies with and without vdW interactions, within the harmonic approximation, using the “frozen phonon” method (FP) or density functional perturbation theory (DFPT). To describe vdW interactions, we adopt the most common approximations: the semiempirical Grimme approximations [Grimme-D2, Grimme-D3, and Grimme-D3-(BJ)];[35,37,38] the Tkatchenko-Scheffler dispersion corrections (TS);[39] and the nonlocal vdW density functional (DFT-vdW) method.[40] We also consider SOC effects in our calculations. For the sake of reproducibility, we run calculations with two different software packages, Quantum EXPRESSO[41] (QE) and ABINIT.[42,43] On top of these calculations, we evaluate anharmonicity in the normal modes by solving the one-dimensional (1D) and the two-dimensional (2D) nuclear Schrödinger equations, using the finite-displacement method.

Our manuscript is organized as follows. In section 2, we introduce the methods and approximations used to calculate normal modes and to evaluate anharmonicity. In section 3, we present and discuss our results in the following order: we first discuss the performance of the GGA and LDA approximations in describing the vibrational properties of $MAPbI_3$ (section 3.1). We then move to discuss the vibrational properties obtained from scalar-relativistic calculations with and without vdW effects (section 3.2). We discuss our results from fully relativistic calculations with and without vdW corrections (section. 3.3). In section 3.4, we discuss the effect of complete geometry relaxation when including vdW corrections and when moving from scalar to fully relativistic calculations. In section 3.5 and section 3.6, we present our results on phonon−phonon anharmonic couplings within the same vibrational mode and between different modes. Finally, in section 4, we provide our concluding remarks.

2. COMPUTATIONAL DETAILS

We calculate the normal modes in the low-temperature orthorhombic phase of $MAPbI_3$. The choice is made on the basis that (1) the orthorhombic structure of $MAPbI_3$ has been characterized thoroughly by means of X-ray and neutron diffraction experiments, and (2) at variance with the room-temperature (tetragonal) and high-temperature (cubic) phases of $MAPbI_3$, in the orthorhombic phase the organic MA cations exhibit a perfect orientational order.[5,44,45]

We study structural properties using density functional theory (DFT) and vibrational properties using either density functional perturbation theory (DFPT) or the “frozen phonon” (FP) method. We carry out calculations using two widely used software packages: Quantum ESPRESSO[41] (QE) and ABINIT.[42,43] Both packages are based on plane-wave basis sets to represent the electronic wave functions and charge density. We test our calculations with the two most common approximations to the exchange-correlation functional, the generalized gradient approximation (GGA) as proposed by Perdew, Burke, and Ernzerhof (PBE),[46] and the local density approximation (LDA).[47] For the calculations performed with QE, ultrasoft[48] and norm-conserving[49] pseudopotentials are employed to describe the core−valence interaction, with the semicore *d* states taken explicitly into account in the case of the Pb and I atoms; while for the calculations performed with ABINIT, optimized norm-conserving Vanderbilt pseudopotentials (ONCVPSP-PBE) are used.[50] Plane-wave basis sets with converged energy cut-offs of 100 and 400 Ry (40 and 200 Ry) are used for norm-conserving (ultrasoft) pseudopotentials to represent the wave functions and charge density, respectively. The first Brillouin zone is sampled with a 4 × 4 × 4 Monkhorst−Pack **k**-point grid.

We adopt several approaches to take into account vdW interactions in our calculations: the Grimme approximations,[35,37,38] the TS correction,[39] and the vdW density functional method proposed by Kolb et al.[40] The Grimme-D2 and TS methods are based on pairwise atomic potentials of the form C_6/R^6, where C_6 are the dispersion coefficients, and R represents the distance between atoms, whereas the last one uses nonlocal potentials. In the Grimme-D3 method, environment-dependent coefficients are used, and a three-body term is added. A revised method proposed by Becke and Johnson,[51,52] referred to as Grimme-D3(BJ), includes a more physical damping function. In the three Grimme methods, the dispersion coefficients are derived empirically from the atomic polarizabilities and first ionization energies of the atoms. In contrast, in the TS method, these coefficients are derived from first-principles, starting from the electron density. All the methods adopted here are implemented either in QE or in ABINIT (or both).

The atomic positions are optimized until the largest force is smaller than 0.005 eV/Å, using the experimental lattice parameters. In all the cases, the structural optimization is initialized using the experimental coordinates of the Pb, I, H, C, and N atoms reported by Baikie et al.[5] For the sake of completeness, we also compute the vibrational properties for fully optimized structures (i.e., both lattice parameters and atomic coordinates). In this case, we study the effect of vdW corrections and SOC effects on the lattice parameters and on the IR spectrum.

Given the relatively large unit cell, we calculate the vibrational normal modes within the harmonic approximation at the Γ point. For the sake of reproducibility, we carry out some phonon calculations with DFPT or FP using the same set of DFT parameters. Both methods produce very similar normal-mode frequencies, with a maximum deviation of 4 cm^{-1}. The Born charge tensors, static and high-frequency dielectric constants, and infrared intensities are calculated using the same methods as in Pérez-Osorio et al.[24]

We evaluate anharmonic corrections for each individual normal mode as follows. For each mode ν, we first compute the adiabatic potential energy surface (APES) as a function of the normal mode coordinate x_ν, using finite displacements. The atomic displacements of an atom κ along direction α, corresponding to the normal mode coordinate x_ν, are generated using $\Delta\tau_{\kappa\alpha} = (M_0/M_\kappa)^{1/2} e_{\kappa\alpha,\nu} x_\nu$, where M_0 is the average mass over the unit cell (in our specific case, it corresponds to the reduced mass of the MAPbI$_3$ primitive unit cell), M_κ are the nuclear masses, and $e_{\kappa\alpha,\nu}$ are the vibrational eigenmodes. We fit the computed APES to a sixth-order polynomial. We then solve numerically the nuclear Schrödinger equation using

$$-\frac{1}{2M_0}\frac{\partial^2 u}{\partial x_\nu^2} + U(x_\nu)u(x_\nu) = Eu(x_\nu) \tag{1}$$

Here, U denotes the computed APES, u represents the nuclear wave functions, and E the corresponding eigenvalue. In order to solve eq 1, we use the finite-difference method.[53] We obtain the anharmonic frequency of the normal modes as the frequency of the vibrational transition between the second and the first eigenvalues.

In order to determine the corresponding harmonic frequencies, we repeat the above procedure, this time retaining only the terms in the polynomial fit up to second order. The anharmonic correction is defined as the difference between the anharmonic and the harmonic frequency.

For the study of anharmonic phonon−phonon couplings between different normal modes, we consider the two modes with the largest anharmonic corrections. As will be shown in section 3.5, the spinning modes of the MA cations are found to carry considerable anharmonicity. Taking into account this result, we investigate phonon−phonon interactions between these two modes.

We evaluate anharmonic phonon−phonon interactions between two phonons, ν and ν', as follows. We first compute the two-dimensional (2D) APES as a function of the normal mode coordinates of two normal modes, x_ν and $y_{\nu'}$, using the finite-displacement method. Once the 2D APES is computed, we fit the data using a 12th-order polynomial of two variables, whose terms are given in Table 1. This 12th-order polynomial is constructed as the product of two sixth-order polynomials, $p(x)$ and $p(y)$. We then solve numerically the 2D nuclear Schrödinger equation, using the finite-difference method:

$$-\frac{1}{2M_0}\left(\frac{\partial^2 u}{\partial x_\nu^2} + \frac{\partial^2 u}{\partial y_{\nu'}^2}\right) + U(x_\nu, y_{\nu'})u(x_\nu, y_{\nu'}) = Eu(x_\nu, y_{\nu'}) \tag{2}$$

This equation is similar to eq 1; however, here U is the computed 2D APES, and u denotes the 2D nuclear wave function. We obtain the anharmonic frequency of the interacting phonons as the difference between the second and the first eigenvalue.

Table 1. Terms of the 12th-Order Polynomial Used to Fit the Computed Two-Dimensional APES[a]

	1	x	x^2	x^3	x^4	x^5	x^6
1	a_{00}	a_{01}x	a_{02}x^2	a_{03}x^3	a_{04}x^4	a_{05}5x^5	a_{06}x^6
y	a_{10}y	a_{11}xy	a_{12}x^{2}y	a_{13}x^{3}y	a_{14}x^{24}y	a_{15}x^{5}y	a_{16}x^{6}y
y^2	a_{20}y^2	a_{21}xy^2	a_{22}x^{2}y^2	a_{23}x^{3}y^2	a_{24}x^{4}y^2	a_{25}x^{5}y^2	a_{26}x^{6}y^2
y^3	a_{30}y^3	a_{31}xy^3	a_{32}x^{2}y^3	a_{33}x^{3}y^3	a_{34}x^{4}y^3	a_{35}x^{5}y^3	a_{36}x^{6}y^3
y^4	a_{40}y^4	a_{41}xy^4	a_{42}x^{2}y^4	a_{43}x^{3}y^4	a_{44}x^{4}y^4	a_{45}x^{5}y^4	a_{46}x^{6}y^4
y^5	a_{50}y^5	a_{51}xy^5	a_{52}x^{2}y^5	a_{53}x^{3}y^5	a_{54}x^{4}y^5	a_{55}x^{5}y^5	a_{56}x^{6}y^5
y^6	a_{60}y^6	a_{61}xy^6	a_{62}x^{2}y^6	a_{63}x^{3}y^6	a_{64}x^{4}y^6	a_{65}x^{5}y^6	a_{66}x^{6}y^6

[a] The polynomial is constructed as the product of two 6th-degree polynomials, $p(x)$ and $p(y)$. The harmonic APES is calculated by considering the terms of this polynomial up to second order (these terms are highlighted in red).

In order to determine the corresponding harmonic frequency, we repeat the above procedure, this time retaining only the polynomial terms up to second order. These terms are highlighted in red in Table 1. Since within the harmonic approximation phonons are decoupled, this frequency is expected to be very similar to the lowest harmonic frequency of the two individual normal modes, as obtained by solving the 1D Schrödinger equation.

The anharmonic correction arising from intermode phonon−phonon coupling is defined as the difference between the anharmonic frequency of the coupled normal modes, and the lowest calculated anharmonic frequency of the two individual modes, as obtained by solving the 1D Schrödinger equation.

3. RESULTS AND DISCUSSION

3.1. LDA vs GGA. The two most common approximations to the DFT exchange and correlation functional are the local density approximation (LDA)[47] and the generalized-gradient approximation (GGA) of PBE.[54] Here, before introducing vdW corrections into our phonon calculations, we test these two approximations in the calculation of the normal-mode frequencies, using DFPT. To this end, we consider scalar-relativistic (sc) calculations. The calculated frequencies within the LDA and GGA are shown in Figure 1a. As we can see, both approximations produce very similar normal-mode frequencies, with a maximum deviation of 8 cm^{-1}. The analysis of the normal modes of MAPbI$_3$, following the method proposed by Pérez-Osorio et al.,[24] reveals that with either functionals they can be classified as internal vibrations of the MA cations (300−3200 cm^{-1}), libration/translation (60−200 cm^{-1}), and spinning (120−140 cm^{-1}) of these cations, as well as internal vibrations of the PbI$_3$ network (10−110 cm^{-1}). Therefore, LDA and GGA yield very similar total and partial vibrational density of states (vDOS), as shown in Figure 2.

To further assess the performance of the LDA and GGA in describing the vibrational properties of MAPbI$_3$, we calculate the Born effective charge tensors and static and high-frequency dielectric constants. Our results for the Born charge tensors are given in Table 2. We observe small differences between the

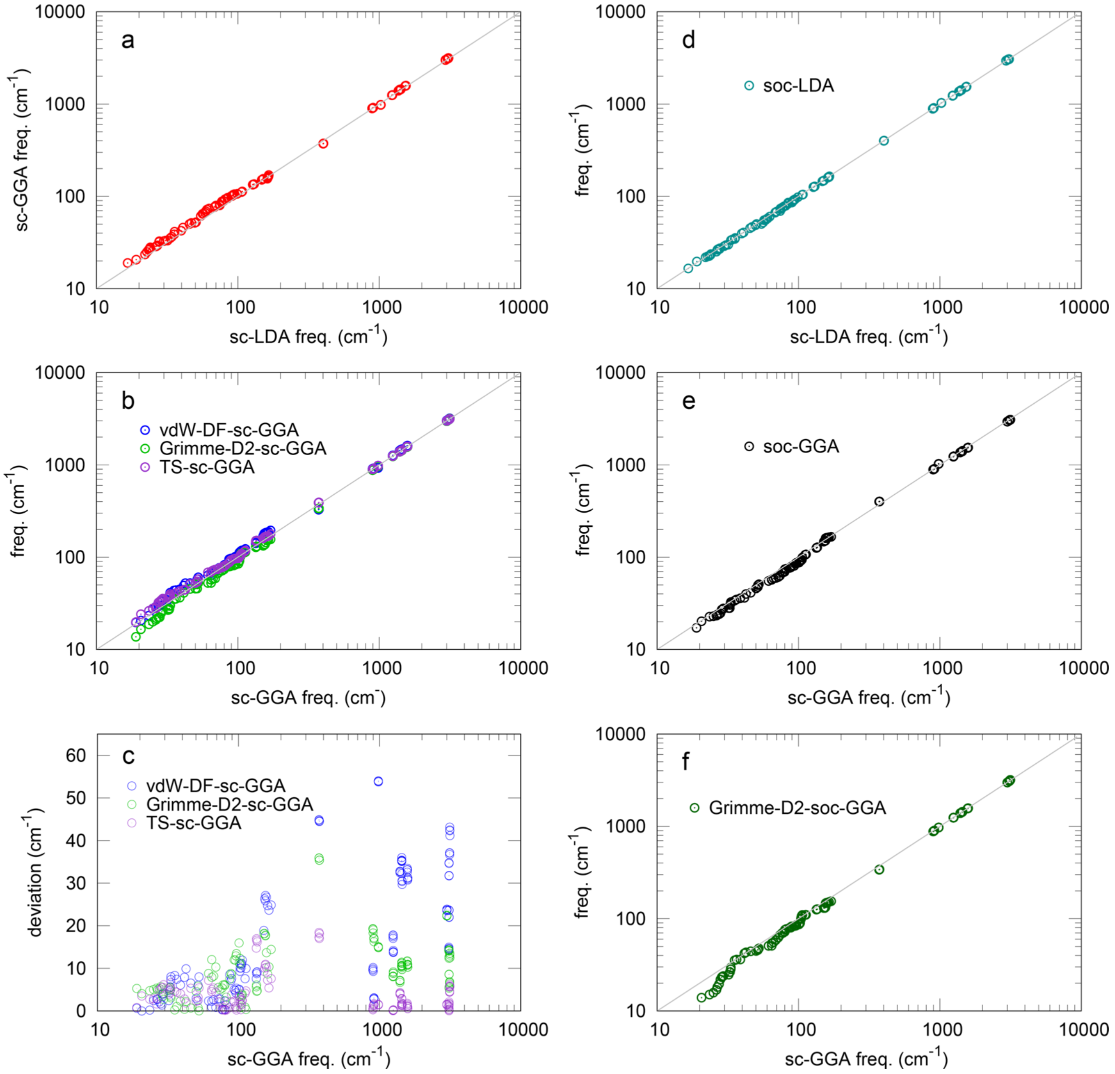

Figure 1. Comparison of the calculated normal-mode frequencies of $MAPbI_3$ with different DFT parametrization schemes: (a) scalar-relativistic calculations using LDA and GGA; (b) scalar-relativistic calculations with vdW corrections, using the GGA; (d and e) fully relativistic calculations using LDA and GGA, respectively; (f) fully relativistic calculations with vdW effects, using the GGA. In b−e, the results are compared with the corresponding calculated frequencies obtained from scalar relativistic calculations without vdW corrections. (c) Deviations of the calculated frequencies with vdW corrections with respect to the corresponding calculated frequencies without vdW corrections. In all the plots, the gray line is a guide to the eye. The calculations were performed using Quantum ESPRESSO.

calculated Born charges with the LDA and GGA approximation. We note that while the Born charge tensor of the Pb atoms is highly isotropic, the Born tensors of the I atoms are very anisotropic. The isotropic averages of the Pb and I Born charge tensors, $\overline{Z}^* = (1/3)\sum_{\alpha} Z^*_{\alpha\alpha}$, are 4.44 (4.37; 4.31) and −1.88 (−1.87; − 1.83), respectively, using LDA within QE (GGA-QE; GGA-ABINIT). These values are larger than the corresponding nominal charges of the Pb and I atoms in $MAPbI_3$, which are +2 and −1, respectively, indicating the mixed covalent-ionic character of the Pb−I bonds. In the case of the C, N, and H atoms, their Born charge tensors are also highly anisotropic. The isotropic averages of the C and N tensors are 0.04 (0.13; 0.12) and −0.92 (−0.84; − 0.81), respectively, with LDA-QE (GGA-QE; GGA-ABINIT). Our calculations yield a high-frequency dielectric constant $\varepsilon_\infty = 5.8$ (5.6; 5.2) using LDA-QE (GGA-QE; GGA-ABINIT). These values for ε_∞ are in good agreement with previous theoretical works[10,21,55] and with the experimental value of 6.5.[56] We further evaluate the static dielectric constant, obtaining a value of $\varepsilon_0 = 25.3$ (20.0; 18.7) using LDA-QE (GGA-QE; GGA-ABINIT). These values are in reasonable agreement with the experimental value of 30.5 measured at 126 K.[57] The fact that the LDA and GGA yield similar results for the normal-mode frequencies and Born effective charges suggests that the infrared spectra of $MAPbI_3$ calculated within these approximations should also be very similar. We verify this hypothesis by explicitly calculating the infrared spectrum using the GGA approximation and comparing our result with the infrared spectrum calculated using the LDA approximation, recently reported by Pérez-Osorio et al.[24] (see Figure 3). We note that the IR peaks in the LDA and GGA calculations match closely. The analysis of the normal modes reveals that the character and symmetry of the peaks are the same. The complete characterization of the peaks was reported by Pérez-Osorio et al.[24] using the LDA approximation. By comparing our calculated infrared spectra with the experimental data of $MAPbI_3$ (see Figure 3), we observe that for most of the measured peaks there is good agreement with our calculated spectra, except for the two peaks

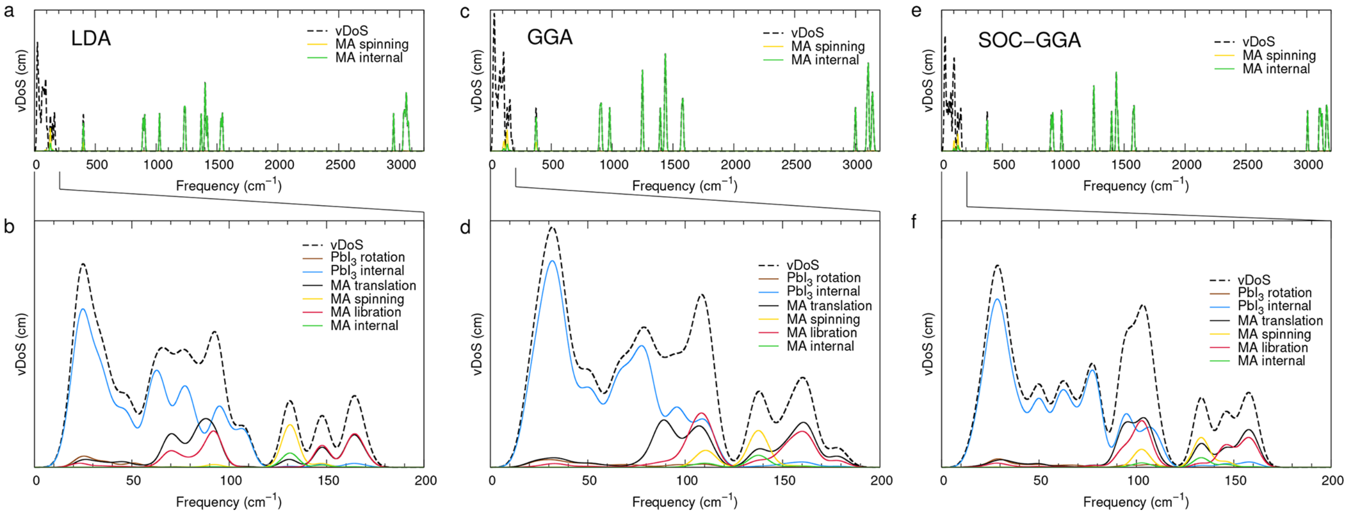

Figure 2. Total and partial vDOS of $MAPbI_3$ over the entire frequency range 0−3200 cm^{-1}, using (a,b) LDA; (c,d) GGA; (e,f) SOC-GGA. (b, d, and f) Details of the total and partial vDOS in the range 0−200 cm^{-1}. The green and blue curves are the internal vibrations of MA and PbI_3, respectively; the yellow, red, and black curves are the spinning, librations, and translations of MA, respectively; the brown curve is the rotations of the PbI_3 octahedra. The total vDOS is shown as a thin dashed black line. We use a Gaussian smearing of 5 cm^{-1} throughout. The calculations were performed using Quantum ESPRESSO.

Table 2. Calculated Born Effective Charges of $MAPbI_3$ within the LDA and GGA Approximations[a]

		LDA-QE			GGA-QE			GGA-ABINIT		
species	WS	Z_1^*	Z_2^*	Z_3^*	Z_1^*	Z_2^*	Z_3^*	Z_1^*	Z_2^*	Z_3^*
Pb	4b	4.21	4.40	4.72	4.04	4.32	4.73	3.77	4.37	4.79
I1	4c	−4.16	−0.96	−0.55	−4.14	−0.95	−0.56	−3.45	−0.87	−0.59
I2	8d	−4.11	−0.93	−0.59	−4.02	−0.92	−0.61	−4.02	−1.00	−0.75
C	4c	−0.16	−0.10	0.39	−0.05	−0.03	0.47	−0.16	0.02	0.50
N	4c	−1.22	−1.00	−0.54	−1.09	−0.93	−0.50	−1.06	−0.85	−0.53
$H1_C$	4c	0.06	0.08	0.02	0.07	0.19	0.19	0.04	0.09	0.14
$H2_C$	8d	0.07	0.15	0.19	0.03	0.12	0.17	0.05	0.13	0.17
$H1_N$	4c	0.11	0.17	1.36	0.12	0.15	1.31	0.17	0.20	1.16
$H2_N$	8d	0.09	0.26	1.32	0.09	0.25	1.26	0.19	0.26	1.09

[a] We report the average of the Born charge tensor eigenvalues $\mathbf{Z}_\alpha^*$ over the atoms in the same Wyckoff site. "QE" and "ABINIT" refer to the software package used in the calculations.

appearing between 150 and 175 cm^{-1}, which correspond to librations of the MA cations. Thus, we find that both the LDA and GGA approximations overestimate the frequencies of these vibrational modes, as previously reported by Pérez-Osorio et al.[24] using the LDA approximation. In the following sections, we investigate whether this overestimation can be attributed to the lack of vdW interactions, SOC effects, and anharmonicity in our phonon calculations.

3.2. vdW Interactions. As the next step, we carry out scalar-relativistic phonon calculations containing vdW corrections. In this case, we employ the FP method and the DFPT approach with QE and ABINIT, respectively. The calculations are performed starting from the GGA approximation of Perdew, Burke and Ernzerhof (PBE):[46] in previous works it was found that the pairwise corrections applied to the PBE exchange-correlation functional work remarkably well in describing the crystal structure of vdW materials.[35,37,39,58−60] The normal-mode frequencies calculated using the Grimme-D2 method, the TS method, and the vdW density functional are displayed in Figure 1b. In this figure the normal-mode frequencies are compared to those calculated without vdW corrections. This allows us to clearly discern the effect of the vdW corrections on the normal-mode frequencies. We observe that the three approaches used to describe vdW corrections, yield normal-mode frequencies that vary slightly from the GGA values without vdW effects. The largest deviations in the low (0−200 cm^{-1}) and high-frequency (400−3200 cm^{-1}) regions are obtained with the vdW-DF method, which yields 25 and 50 cm^{-1}, respectively, as shown in Figure 1c. With the TS method (Grimme-D2), the largest deviations in the low and high-frequency regions are 15 and 20 cm^{-1} (15 and 35 cm^{-1}), respectively [see Figure 1c].

Normal mode frequencies calculated with Grimme-D3 and Grimme-D3(BJ) methods are similar to the Grimme-D2 values. The largest deviation from the GGA values in the low and high-frequency regions are 20 and 40 cm^{-1} (∼15% and ∼1.5%), respectively, with Grimme-D3, and 10 and 30 cm^{-1} (∼7% and ∼1%), respectively, with Grimme-D3(BJ). Therefore, our results strongly support the notion that vdW interactions have only little effect on the vibrational properties of $MAPbI_3$.

To further clarify this point, we calculate Born charge tensors, dielectric constants, and infrared spectra of $MAPbI_3$ by including vdW corrections. Our results for the Born charge tensors calculated using ABINIT within the Grimme-D2, Grimme-D3 and Grimme-D3(BJ) approximations are given in Table 3. We observe small differences between the calculated

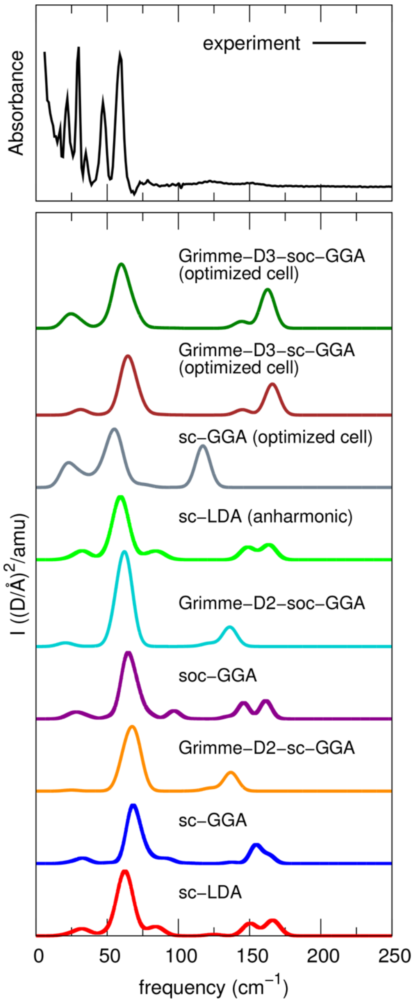

Figure 3. Infrared spectra of $MAPbI_3$, in the low frequency region, calculated at the experimental and at optimized lattice parameters, using different functionals. Spectra calculated at experimental lattice parameters: scalar-relativistic LDA and GGA (red and blue curves, respectively); scalar-relativistic GGA with Grimme-D2 vdW corrections (orange curve); fully relativistic GGA (purple curve); fully relativistic GGA with Grimme-D2 vdW corrections (light blue curve); scalar-relativistic LDA with anharmonic corrections to the normal-mode frequencies (green curve). Spectra calculated at optimized lattice parameters: scalar-relativistic GGA (gray curve), scalar-relativistic GGA with Grimme D3 vdW corrections (brown curve), and fully relativistic GGA with Grimme-D3 vdW corrections (dark green curve). The spectra are calculated using a Gaussian broadening of 5 cm^{-1}. The explicit expression for the infrared intensity can be found in the work by Pérez-Osorio et al.,[24] eq (4). For comparison, we show the experimental spectrum reported by Pérez-Osorio et al.[24] Reprinted from ref 24. Copyright 2015 American Chemical Society. The calculations were performed using Quantum ESPRESSO [sc-LDA, sc-GGA, soc-GGA, and sc-LDA(anharmonic)] and ABINIT [Grimme-D2-sc-GGA, Grimme-D2-soc-GGA, sc-GGA (optimized cell), Grimme-D3-sc-GGA (optimized cell), and Grimme-D3-soc-GGA (optimized cell)].

Born charges with and without vdW corrections. The isotropic average of the Pb, I, C, and N Born effective charge tensors are 4.34, − 1.85, 0.13, and −0.78, respectively, using Grimme-D2; 4.22, −1.80, 0.11, and −0.83, respectively, using Grimme-D3; and 4.28, −1.81, 0.12, and −0.82, respectively, using Grimme-D3(BJ). The three methods produce very similar Born effective charge tensors, with the largest deviation found for the Pb atoms. Our calculations yield a high-frequency dielectric constant ε_∞ = 5.5, 5.1, or 5.2, using the Grimme-D2, Grimme-D3, or Grimme-D3(BJ) approximation, respectively. Our static dielectric constant is ε_0 = 25.3, 21.0, or 18.2, using Grimme-D2, Grimme-D3, or Grimme-D3(BJ), respectively. All these values are close to our GGA results without vdW corrections (ε_∞ = 5.6 and ε_0 = 20.0), and remain in reasonable agreement with the experimental values of 6.5[56] and 30.5.[57] Figure 3 shows that our calculated infrared spectra of $MAPbI_3$ obtained by including vdW corrections are very similar to the spectrum obtained within the GGA approximation (without vdW corrections). Neither the intensity nor the position of the peaks is significantly modified. The two peaks appearing between 150 and 175 cm^{-1} are slightly red-shifted, by at most 15 cm^{-1}, reducing the discrepancy with the experimental spectrum.

Overall, we find that the results obtained with the different methods used to account for the vdW interactions are consistent. Moreover, our results reveal that the inclusion of vdW effects in the calculations do not change in any significant way the vibrational frequencies and the infrared spectrum of $MAPbI_3$. These results strongly support the idea that vdW interactions do not play an important role in the vibrational properties of this perovskite.

In the next section, we investigate whether SOC effects in combination with vdW interactions could produce non-negligible changes.

3.3. vdW Interactions and SOC Effects.

It is well-known that to correctly describe the electronic properties of $MAPbI_3$ from first-principles, it is important to take into account spin−orbit interactions. The calculated scalar-relativistic bandgap of $MAPbI_3$ is 1.68 eV,[10] which is coincidentally very close to the experimental optical bandgap 1.6 eV.[61] This is an artifact due to the neglect of spin−orbit interactions of the Pb and I atoms in the calculation. On the contrary, the calculated band gap within fully relativistic DFT is 0.6 eV.[10] By including quasiparticle corrections on top of the fully relativistic DFT calculation via the state-of-the-art GW approximation and by performing self-consistency on the eigenvalues, the bandgap becomes 1.72 eV,[62] which is in good agreement with the experiment.

In this section, we investigate whether the spin−orbit coupling in combination with vdW corrections has an effect on the vibrational properties of $MAPbI_3$. As the first step, we analyze the normal-mode frequencies. To distinguish the effects arising from SOC corrections and from vdW interactions, we perform fully relativistic phonon calculations with and without vdW effects. In Figure 1d and e, we compare our calculated fully relativistic normal-mode frequencies without vdW effects with our results from scalar-relativistic calculations, using the LDA and GGA approximations, respectively. One can observe in Figure 1d and e that the differences between the scalar and fully relativistic normal-mode frequencies are small, both in the LDA and GGA. The largest deviations in the low and high-frequency regions are 5 and 20 cm^{-1}, respectively, with LDA, and 15 and 40 cm^{-1}, respectively, with GGA. These results point to the fact that the vibrational modes of the Pb−I network and MA cations are not influenced by the strong SOC of the Pb and I atoms. The analysis of the normal modes reveals that the vibrational density of states in the scalar and fully relativistic descriptions are almost the same, as shown in Figure 2e and f.

We then proceed to include vdW corrections in our fully relativistic calculations. To this end, we consider the three

Table 3. Comparison of the Born Effective Charges of $MAPbI_3$ Calculated Using Scalar-Relativistic GGA with or without vdW Corrections [Grimme-D2, Grimme-D3, and Grimme-D3(BJ)][a]

		sc-GGA			Grimme-D2-sc			Grimme-D3-sc			Grimme-D3(BJ)-sc		
species	WS	Z_1^*	Z_2^*	Z_3^*	Z_1^*	Z_2^*	Z_3^*	Z_1^*	Z_2^*	Z_3^*	Z_1^*	Z_2^*	Z_3^*
Pb	4b	3.77	4.37	4.79	3.92	4.14	4.96	3.78	4.18	4.70	3.78	4.28	4.78
I1	4c	−3.45	−0.87	−0.59	−4.40	−0.84	−0.61	−3.48	−0.83	−0.61	−3.45	−0.85	−0.60
I2	8d	−4.02	−1.00	−0.75	−3.91	−0.78	−0.73	−3.87	−0.97	−0.78	−3.97	−0.98	−0.75
C	4c	−0.16	0.02	0.50	−0.17	0.08	0.48	−0.24	0.07	0.49	−0.21	0.06	0.50
N	4c	−1.06	−0.85	−0.53	−1.13	−0.64	−0.57	−1.12	−0.80	−0.57	−1.10	−0.80	−0.55
$H1_C$	4c	0.04	0.09	0.14	0.04	0.07	0.19	0.05	0.08	0.17	0.05	0.07	0.16
$H2_C$	8d	0.05	0.13	0.17	0.07	0.13	0.15	0.08	0.11	0.16	0.07	0.12	0.16
$H1_N$	4c	0.17	0.20	1.16	0.19	0.27	1.10	0.20	0.26	1.07	0.19	0.24	1.11
$H2_N$	8d	0.19	0.26	1.09	0.23	0.39	0.90	0.21	0.31	1.02	0.22	0.27	1.04

[a] We report the average of the Born charge tensor eigenvalues Z_α^* over the atoms in the same Wyckoff site. The calculations were performed using ABINIT.

Table 4. Comparison of the Born Effective Charges of $MAPbI_3$ Calculated Using Fully-Relativistic GGA with or without vdW Corrections [Grimme-D2, Grimme-D3, and Grimme-D3(BJ)][a]

		sc-GGA			soc-GGA			Grimme-D2-soc			Grimme-D3-soc			Grimme-D3(BJ)-soc		
species	WS	Z_1^*	Z_2^*	Z_3^*	Z_1^*	Z_2^*	Z_3^*	Z_1^*	Z_2^*	Z_3^*	Z_1^*	Z_2^*	Z_3^*	Z_1^*	Z_2^*	Z_3^*
Pb	4b	3.77	4.37	4.79	4.07	4.78	5.16	4.31	4.57	5.41	4.08	4.54	5.04	4.07	4.67	5.14
I1	4c	−3.45	−0.87	−0.59	−3.51	−0.91	−0.62	−4.81	−0.85	−0.62	−3.55	−0.86	−0.63	−3.51	−0.89	−0.63
I2	8d	−4.02	−1.00	−0.75	−4.37	−1.07	−0.79	−4.27	−0.79	−0.76	−4.19	−1.03	−0.79	−4.31	−1.05	−0.79
C	4c	−0.16	0.02	0.50	−0.17	0.02	0.50	−0.62	−0.18	1.16	−0.25	0.07	0.48	−0.22	0.06	0.50
N	4c	−1.06	−0.85	−0.53	−1.07	−0.86	−0.53	−1.15	−0.66	−0.57	−1.14	−0.82	−0.56	−1.12	−0.83	−0.55
$H1_C$	4c	0.04	0.09	0.14	0.04	0.09	0.14	0.04	0.07	0.19	0.05	0.08	0.17	0.05	0.08	0.16
$H2_C$	8d	0.05	0.13	0.17	0.05	0.13	0.17	0.07	0.13	0.15	0.08	0.11	0.16	0.07	0.12	0.16
$H1_N$	4c	0.17	0.20	1.16	0.17	0.20	1.16	0.19	0.27	1.11	0.20	0.25	1.09	0.18	0.24	1.12
$H2_N$	8d	0.19	0.26	1.09	0.18	0.26	1.10	0.23	0.39	0.91	0.21	0.30	1.04	0.22	0.27	1.05

[a] Scalar-relativistic results using GGA are also reported for comparison. We report the average of the Born charge tensor eigenvalues Z_α^* over the atoms in the same Wyckoff site. The calculations were performed using ABINIT.

Table 5. Scalar and Fully-Relativistic High-Frequency (ε^∞) and Static (ε^0) Dielectric Constants of $MAPbI_3$ Calculated within the LDA and GGA Approximations, with or without vdW Corrections [Grimme-D2, Grimme-D3, and Grimme-D3(BJ)][a]

	LDA-QE	GGA-QE		GGA-ABINIT							
						sc	sc	sc	soc	soc	soc
	sc	sc	soc	sc	soc	Grimme-D2	Grimme-D3	Grimme-D3(BJ)	Grimme-D2	Grimme-D3	Grimme-D3(BJ)
ε^∞	5.8	5.6	6.8	5.2	5.9	5.5	5.1	5.2	6.4	5.7	5.8
ε^0	25.3	20.0	27.2	18.7	25.3	25.3	21.0	18.2	30.3	31.5	24.9

[a] "QE" and "ABINIT" refer to the software package used in the calculations.

Grimme approaches and the GGA approximation. The frequencies resulting from the Grimme-D2 method are shown in Figure 1f, where they are compared with our scalar-relativistic frequencies using GGA. We observe that the calculated fully relativistic frequencies with vdW effects vary only slightly with respect to the scalar-relativistic frequencies. The largest deviations in the low and high-frequency regions are of 15 and 40 cm^{-1}, respectively. The same calculations performed with Grimme-D3 and Grimme-D3(BJ) lead to deviations in the low and high-frequency regions of at most 20 and 35 cm^{-1}, respectively, with Grimme-D3 and 10 and 30 cm^{-1}, respectively, with Grimme-D3(BJ). Therefore, the inclusion of relativistic effects and vdW corrections in our calculations does not have any significant effects on the normal-mode frequencies.

We also calculated the Born effective charge tensors, dielectric constants, and infrared spectra of $MAPbI_3$ with SOC effects, with and without vdW corrections. Our results for the fully relativistic Born effective charge tensors are given in Table 4. These results are very similar to the scalar-relativistic values. The isotropic averages of the C, N, and H Born effective charge tensors are not modified by the strong SOC of the Pb and I atoms. However, the isotropic averages of the Pb and I Born effective charge tensors become 4.67 and −1.94, corresponding to variations of 8 and 6%, respectively, with respect to the scalar-relativistic values. As in section 3.2, we found that the inclusion of vdW corrections in our fully relativistic calculations yields only small modifications of the Born effective charge tensors. More precisely, the variations from GGA to Grimme-vdW are very similar for both scalar and fully relativistic calculations. All the variants of the Grimme approximation are consistent. Our fully relativistic calculations yield high-frequency and static dielectric constants of $\varepsilon_\infty = 5.9$ (6.8) and $\varepsilon_0 = 25.3$ (27.2), respectively, using GGA-ABINIT (GGA-QE). The implementation of both vdW corrections and SOC effects lead to $\varepsilon_\infty = 6.4$ (5.7; 5.8) and $\varepsilon_0 = 30.3$ (31.5;

24.9), using Grimme-D2 [Grimme-D3; Grimme-D3(BJ)] to account for the vdW interactions, with GGA-ABINIT. For clarity, all the calculated dielectric constants are summarized in Table 5. The fact that both scalar-relativistic and fully relativistic approaches yield similar results for normal-mode frequencies, Born effective charge tensors, and dielectric constants of $MAPbI_3$ suggests that the calculated infrared spectrum of $MAPbI_3$ should not be significantly affected by the inclusion of SOC effects. We verified this hypothesis and found that the IR peaks with and without SOC effects match closely, in terms of position and intensity of each peak. This is shown in Figure 3. The largest shift in the low-frequency region is 5 cm^{-1}. The shifts arising from SOC effects are, therefore, smaller than the ones due to the inclusion of vdW corrections. The fully relativistic calculation including vdW effects leads to a maximum red shift of 20 cm^{-1} in the low-frequency region, which does not significantly reduce the discrepancy between theory and IR experiments.

3.4. Optimization of the Unit Cell.

Up to this point, all calculations have been performed for a structure where only the atomic positions are optimized, while keeping the lattice parameters fixed at their experimental values. Under such conditions, our results indicate that the vibrational properties are neither modified by vdW corrections nor by SOC effects.

In this section, we also perform calculations for fully relaxed structures with and without dispersive corrections and SOC effects. First, the results obtained from scalar-relativistic calculations at experimental lattice parameters are compared to those from scalar-relativistic calculations at relaxed lattice parameters. Then, vdW corrections are included using the Grimme-D3 approximation, and effects on both lattice parameters and vibrational properties are discussed. Finally, results from fully relativistic calculations performed at relaxed lattice constants are presented.

Table 6 summarizes the computed lattice parameters and their relative differences with respect to the experimental values. First of all, the relaxed lattice parameters from scalar-relativistic GGA calculations without vdW corrections are larger than the experimental values in the three directions, with a maximum deviation of 5.7% along the *c*-axis and a small deviation of 0.2% along the *a*-axis. Regarding the vibrational properties, we observe a global red shift of the IR spectrum by at most 25 cm^{-1} (see Figure 3). This is not surprising given that an increase of the unit cell usually leads to a decrease of the normal-mode frequencies (except for modes with negative Grüneisen parameter).

Table 6. Optimized Lattice Parameters (in Å) of $MAPbI_3$ Calculated within Scalar and Fully-Relativistic Parametrizations with and without Grimme-D3 vdW Corrections[a]

		relaxed			
	experimental	sc-GGA	Grimme-D3-sc	soc-GGA	Grimme-D3-soc
a	8.56	8.58 (+0.2%)	8.41 (−1.8%)	8.60 (+0.5%)	8.41 (−1.8%)
b	12.58	12.91 (+2.6%)	12.75 (+1.4%)	12.91 (+2.6%)	12.74 (+1.3%)
c	8.84	9.34 (+5.7%)	9.01 (+1.9%)	9.36 (+5.9%)	9.02 (+2.0%)

[a] For comparison, the experimental lattice parameters are also reported, and the relative deviations are given in parentheses.

The relaxed lattice parameters computed using the Grimme-D3 method are smaller than the relaxed GGA values without vdW interactions and closer to the experimental lattice parameters (along the *b* and *c* axes) with a maximum deviation of 1.9%. Therefore, we find a global blue shift of the IR spectrum by at most 50 cm^{-1} (see Figure 3). Moreover, if we compare the theoretical IR spectrum for the relaxed structure computed using the Grimme-D3 method with the theoretical IR spectrum computed with GGA at experimental lattice parameters, we see that the peaks at frequencies lower than 100 cm^{-1} and higher than 120 cm^{-1} are respectively red-shifted and blue shifted. This difference comes from the origin of the IR peaks. The former peaks are mainly due to normal modes of B_{2u} and B_{1u} symmetry (vibrations in y and z directions), while the latter peaks come from normal modes with B_{3u} symmetry (vibrations in x direction). As the relaxed lattice parameter in the x direction (a) computed within the Grimme-D3 approach is smaller than the experimental value, the frequencies tend to be higher. In contrast, the relaxed lattice parameters in the y and z directions (b and c) are larger than the experimental values, explaining the shift toward lower frequencies. In conclusion, while the inclusion of vdW interactions improves the agreement with experiment for two of the lattice parameters, the influence on the IR spectrum is not significant.

Finally, fully relativistic calculations do not lead to noticeable modifications of the lattice parameters. Indeed, scalar and fully relativistic calculations lead to similar, if not equal, lattice constants, whether with or without vdW corrections. As a consequence, the IR spectra computed at relaxed parameters with and without relativistic effects are almost identical (see Figure 3). The small red shift of the IR spectrum is not far from the one reported in section 3.3 and is mainly due to the modification of the atomic positions in the unit cell.

The results presented in this section show that the optimization of the unit cell only plays a limited role on the vibrational properties. Indeed, compared to the experimental lattice parameters, the theoretical values differ by less than 6% within GGA and 2% when including vdW corrections (SOC effects are completely negligible at that level), leading to a maximum shift of 25 cm^{-1} with respect to the results of previous sections. All the low-frequency modes present positive Grüneisen parameters, and the vibrational frequencies calculated at the experimental lattice parameters shift according to the change in the lattice parameters and depending on their symmetry. Our finding that vdW forces do not influence significantly the IR spectrum of $MAPbI_3$ is in line with the notion that interactions between the organic MA cations and the inorganic PbI_3 network are mainly electrostatic in nature. This observation is consistent with the recent work of Mattoni et al.,[23,63,64] where the authors investigated the vibrational properties of $MAPbI_3$ using classical molecular dynamics simulations. In these studies, the authors found that using ionic Buckhingham−Coulomb potentials is sufficient to correctly describe the vibrational properties of $MAPbI_3$.

The results of section 3.3 and the present section indicate that vdW forces and SOC corrections do not account for the overestimation of the librations of MA. Therefore, we proceeded to check whether anharmonic effects may be the origin of the apparent discrepancy between theory and experiment.

3.5. Anharmonic Phonon−Phonon Coupling within the Same Mode.

Of all the phonon calculations with the various DFT parametrization schemes carried out in section 3, we choose the most representative ones to evaluate anharmonicity. Thus, we consider scalar-relativistic calculations with and without vdW interactions, namely, sc-LDA and TS-sc-GGA, respectively, and a fully relativistic calculation (SOC-LDA). As a validation test for the sc-LDA calculation, we compare the harmonic frequencies calculated by solving the nuclear Schrödinger equation with the corresponding frequencies obtained from the FP calculation. Our results for the first 72 normal modes with lowest frequencies (which include the internal vibrations of the PbI_3 network and the libration and spinning of the MA cations) are shown in Figure 4. As we can see, both methods produce almost the same frequencies, with the largest deviations being smaller than 5 cm^{-1} (0.6 meV). We repeat the same validation test for the other two representative phonon calculations and obtain similar results.

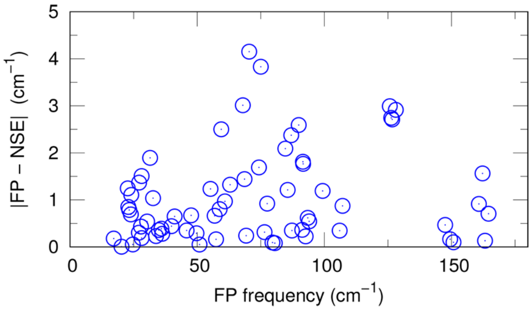

Figure 4. Difference between the frequencies obtained by diagonalizing the dynamical matrix from FP and those obtained from the solution of the nuclear Schrödinger equation (sc-LDA).

Having validated the FP method, we proceed to evaluate anharmonic corrections. The anharmonic and harmonic APES of a representative normal mode, along with the corresponding first three eigenfunctions are shown in Figure 5a. The normal mode corresponds to one of the spinning modes of the MA cations in $MAPbI_3$. We start with the scalar-relativistic frequencies (sc-LDA), whose results are shown in Figure 5b. One can observe that for most modes anharmonic effects are practically negligible (within 3 cm^{-1}), except for four modes with frequencies between 120 and 140 cm^{-1}, for which the anharmonic corrections are as large as ~35 cm^{-1}. We find that the modes carrying considerable anharmonicity correspond to spinning of the organic MA cations. In Figure 6, we show a schematic representation of the spinning mode of an isolated MA cation, which is similar to the spinning modes of the MA cation in the perovskite. Similar results are obtained for the fully relativistic normal modes, as shown in Figure 5c. In the case of the scalar-relativistic normal modes with vdW corrections (Figure 5d), we note that more than four normal modes (nine altogether) exhibit considerable anharmonicity, up to 20 cm^{-1}.

The fact that in the three calculations considered here we observe anharmonicity in exactly the same normal modes indicates that anharmonicity is insensitive to relativistic effects and vdW corrections. Going back to the calculated infrared spectrum of $MAPbI_3$, we observe that the anharmonic corrections for the infrared-active librations modes are practically negligible. Regarding the spinning modes of MA cations, although the anharmonic corrections shift these normal modes to higher frequencies by as much as 40 cm^{-1}, this shift does not induce any change in our calculated infrared spectrum of $MAPbI_3$ because the infrared intensities of the spinning modes are very small, as shown in Figure 3.

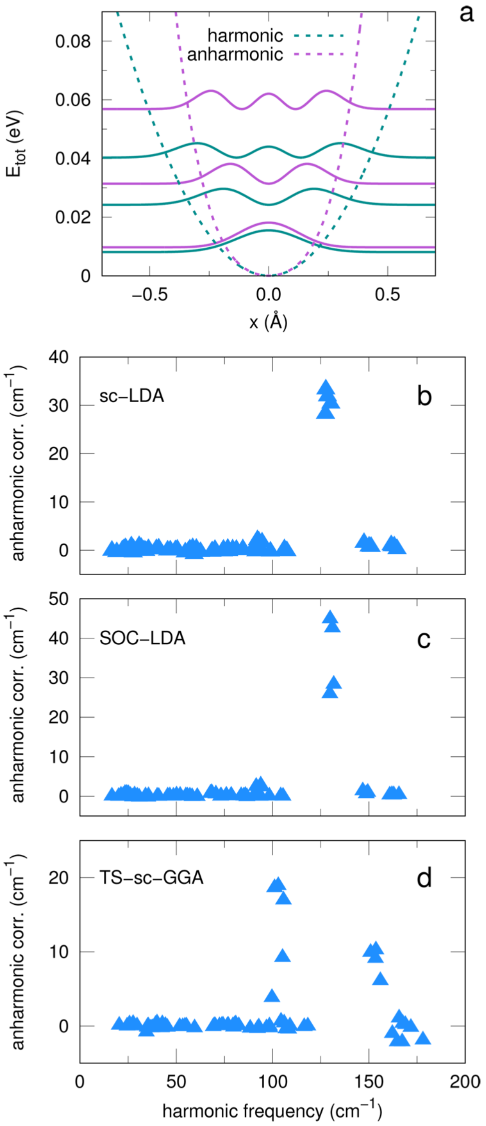

Figure 5. Anharmonic corrections to the normal-mode frequencies of $MAPbI_3$. (a) Harmonic and anharmonic APES of a representative normal mode of $MAPbI_3$, green and purple dashed curve, respectively. The normal mode corresponds to one of the spinning modes of the MA cations in $MAPbI_3$. The first three eigenvalues of the harmonic and anharmonic potential, obtained by solving the 1D nuclear Schrödinger equation, are represented by the green and purple solid curves, respectively. (b and c) Anharmonic corrections to the calculated normal-mode frequencies with and without SOC effects, respectively. In both cases, the LDA approximation is used. (d) Anharmonic corrections to the scalar-relativistic normal-mode frequencies with vdW interactions. The analysis of the normal modes reveals that the normal modes exhibiting considerable anharmonicity in b−d correspond to spinning modes of the organic MA cations. These calculations were performed using Quantum ESPRESSO.

Before moving to the next section, we briefly comment on the physical origin of the anharmonicity of the spinning modes of the MA cations. The spinning modes are directly related with the C_3 jumping rotations of MA cations in the cuboctahedral cage, as they both belong to the same symmetry point group (C_{3v}). Recent inelastic neutron scattering experiments (INS)

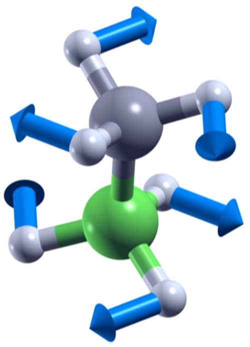

Figure 6. Schematic representation of the spinning mode of an isolated MA cation. The MA cation is represented by a ball-and-stick model, with the C, N, and H atoms in green, gray, and white, respectively. The displacements of the H atoms are indicated by the blue arrows.

have revealed that the C_3 jumping rotations are active in the low-temperature phase of $MAPbI_3$ (with an activation energy of 48 meV), whereas the C_4 jumping rotations (which are related with the libration modes of the MA cations) are frozen in this phase.[65,66] These observations suggest that the anharmonicity of the spinnning modes of the MA cations may originate from the small activation barrier of C_3 jumping rotations.

3.6. Anharmonic Phonon−Phonon Coupling between Different Modes.

In this section we investigate phonon−phonon anharmonic couplings between different normal modes. To this aim we select the spinning modes of the MA cations, on the grounds that these normal modes are the only ones which exhibit significant anharmonicity (see section 3.5). We consider the modes with harmonic frequencies 128.7 and 129.0 cm^{-1} in LDA (see Figure 5b), and compute their 2D APES within the same approximation. In Figure 7, we compare the anharmonic and the harmonic 2D APES resulting from the polynomial fit described in section 2. Since the spinning modes are almost degenerate in frequency, we found that the second and third eigenvalues obtained using either the anharmonic or the harmonic 2D APES are almost degenerate. For this reason, we consider the average between these two eigenvalues to evaluate the frequencies of the coupled modes.

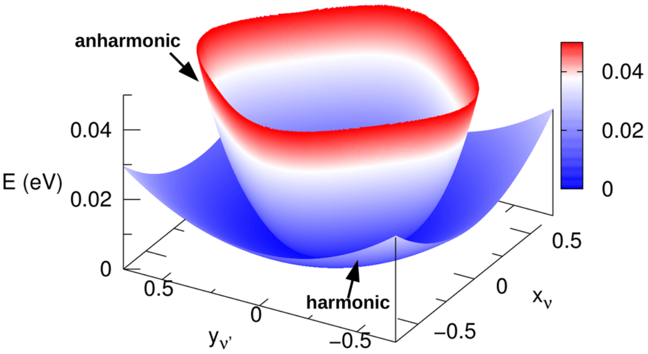

Figure 7. Anharmonic and harmonic 2D APES for the coupled spinning modes of the MA cations, with individual harmonic frequencies of 128.7 and 129.0 cm^{-1} in LDA.

As a sanity check, we verified that if we retain only the second order terms in the polynomial fit of the 2D APES, we correctly obtain the harmonic frequencies. In line with this expectation, we found that the difference between the harmonic frequency of the coupled phonons and the average of the harmonic frequencies of the individual phonons is smaller than 0.1 cm^{-1}.

Having validated the methodology, we proceed to calculate the anharmonic corrections due to phonon−phonon interactions between the two spinning modes. We quantify the correction by evaluating $\Delta\hbar\omega$ from the expression $E_2 + E_1 - 2E_0 = \hbar\omega_1 + \hbar\omega_2 + 2\Delta\hbar\omega$, with E_0, E_1, and E_2 the ground state and the first and second excited states, respectively, and $\hbar\omega_1$ and $\hbar\omega_2$ are the anharmonic frequencies without intermode coupling. We found that the correction is relatively small, $\Delta\omega$ = 18 cm^{-1}, and amounts to approximately half of the anharmonic correction arising from intramode phonon−phonon coupling evaluated in section 3.5.

Since the spinning modes exhibit by far the largest anharmonic corrections when the intermode coupling is neglected, we expect the phonon−phonon coupling to be even smaller for all the other normal modes. Therefore, our results indicate that anharmonic phonon−phonon coupling between different normal modes does not play an important role in the vibrational properties of $MAPbI_3$.

4. CONCLUSIONS

In the present work, we performed a systematic study of the effects of vdW interactions, SOC corrections, and anharmonicity on the vibrational properties of $MAPbI_3$. To this end, we carried out several calculations with different DFT parametrization schemes: scalar-relativistic phonon calculations with and without vdW corrections, and fully relativistic phonon calculations with and without vdW corrections. To account for the vdW interactions, we adopted several approximations: three Grimme methods, the TS correction, and the vdW density

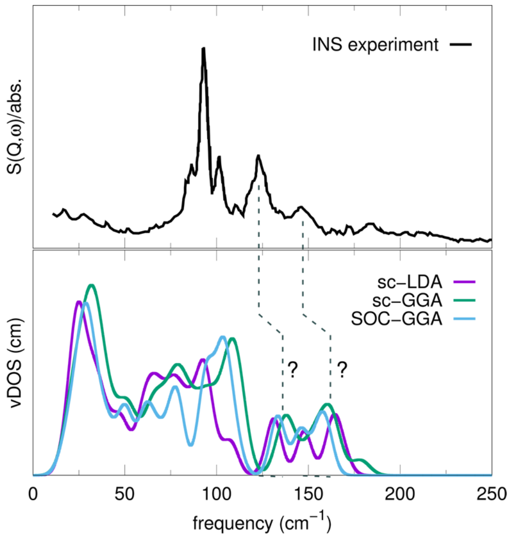

Figure 8. Comparison between the experimental INS spectrum of $MAPbI_3$ (black curve), recently reported by Druzbicki et al.,[67] and our calculated vDOS for this perovskite, using the scalar-relativistic LDA and GGA (purple and green curves, respectively), and fully relativistic GGA (blue curve) (calculations using Quantum ESPRESSO). The black dashed lines denote our tentative assignment of the broad peaks at 123 and 147 cm^{-1} in the INS spectrum to our calculated spinning and libration modes of MA cations, with frequencies between 125 and 175 cm^{-1}. We note that Druzbicki et al.[67] propose a slightly different assignment of these two features, suggesting that they are both associated with MA librations.

functional. We checked our results within the LDA and GGA approximations, and we compared the results of two codes, QE and ABINIT. We also evaluated the anharmonicity of the calculated normal modes by solving the nuclear Schrödinger equation, using finite displacements.

Our scalar-relativistic calculations showed that the LDA and GGA approximations work remarkably well in describing the vibrational properties of $MAPbI_3$, as they both yield very similar results. The comparison of the calculated scalar-relativistic infrared spectra using LDA and GGA with the experimental data reported by Pérez-Osorio et al.[24] revealed that for most of the calculated peaks there is a good agreement with experiment, except for the peaks assigned to librations of the MA cations, which appear at higher frequencies with respect to experiment.

The inclusion of vdW corrections in our scalar-relativistic calculations does not induce any significant change in the normal-mode frequencies. Moreover, no significant change in Born charge tensors and dielectric constants was observed. Hence, the frequencies of the MA-cation librations are not significantly affected by vdW corrections. We found that our fully relativistic calculations with and without vdW corrections yield normal-mode frequencies very similar to those obtained in our scalar-relativistic calculations. These results hold for both QE and ABINIT calculations. Also, Born effective charge tensors and dielectric constants are almost unmodified. Moreover, neither the position nor the intensity of the IR peaks is significantly changed. Therefore, the inclusion of SOC effects in our calculations does not account for the apparent overestimation of the libration modes in the IR spectrum. Calculations performed at relaxed lattice parameters lead to the same conclusion. Although on average the lattice parameters get closer to the experimental values when including vdW interactions, the IR spectrum is not significantly modified. Taken together, our results indicate that the vibrational properties of $MAPbI_3$ are neither sensitive to vdW corrections nor to SOC corrections (within 10−20 cm^{-1}).

In the last part of this work, we checked whether anharmonicity plays a role on the normal-mode frequencies of $MAPbI_3$, in particular on the librations of the MA cations. We found that for most vibrational modes, the anharmonic corrections are negligible, including the librations of MA, except for the spinning modes of these organic cations, for which the anharmonic corrections are as large as 35 cm^{-1}. However, the anharmonic frequencies of the spinning modes do not induce any significant change in the infrared spectrum since these normal modes have small IR activity.

We also found that anharmonic phonon−phonon couplings between different modes in $MAPbI_3$ are relatively small, the largest correction arising from these effects being less than 20 cm^{-1}.

In summary, our study shows that vdW forces, SOC effects, anharmonicity, and phonon−phonon interactions do not play an important role in the vibrational properties of $MAPbI_3$. Therefore, the discrepancy between the peaks at 155 and 175 cm^{-1} in the calculated infrared spectrum, arising from librations of the MA cations, and the experimental infrared data reported by Pérez-Osorio et al.[24] remains. In this regard, we point out that the said discrepancy may also be attributed to a mismatch in the IR intensities since the experiments reported in ref 24 show some very small but nonzero signals in the frequency range where our calculations place librational excitations.

We also note that recently Druzbicki et al.[67] investigated the vibrational properties of $MAPbI_3$ using INS spectroscopy, an experimental technique that provides information on the vibrational density of states (vDOS). The comparison between the INS spectrum of $MAPbI_3$, measured by Druzbicki et al.,[67] and our calculated vDOS for this perovskite, in the low-frequency region (see Figure 8), shows that there is a reasonably good agreement between experiment and theory, not only for the internal vibrations of the Pb−I network (with frequencies between 0−75 cm^{-1}) but also for the spinning and librations modes of the MA cations (with frequencies between 75−190 cm^{-1}), including those libration modes at 155 and 175 cm^{-1}. Therefore, these new INS studies support the notion that our calculated normal-mode frequencies for $MAPbI_3$ are reasonably accurate and reliable. This reinforces the possibility that the discrepancy between the experimental and calculated infrared spectra in the libration region may relate to the IR intensities, as opposed to the frequencies. The residual discrepancy between the calculated and measured IR intensities remains an outstanding question and calls for further investigations, both on the theory front and on the experimental front. High-resolution Raman data could help resolve this question.

■ AUTHOR INFORMATION

Corresponding Author

*E-mail: feliciano.giustino@materials.ox.ac.uk.

ORCID

Feliciano Giustino: 0000-0001-9293-1176

Notes

The authors declare no competing financial interest.

■ ACKNOWLEDGMENTS

This work was supported by the UK Engineering and Physical Sciences Research Council (Grant Numbers EP/J009857/1 and EP/M020517/1) and the Leverhulme Trust (Grant RL-2012-001). The research leading to these results has received funding from the European Union H2020 Programme under grant agreement number 696656-Graphene-Core1. This work used the ARCHER UK National Supercomputing Service and the Advanced Research Computing facility of the University of Oxford. It has also been supported by the UCL through a FSR grant (to A.C.). Computational resources were also provided by the supercomputing facilities of the Université catholique de Louvain (CISM/UCL) and the Consortium des Equipements de Calcul Intensif en Fédération Wallonie Bruxelles (CECI) funded by the Fonds de la Recherche Scientifique de Belgique (F.R.S.-FNRS) under convention 2.5020.11. All structural models were rendered using VESTA.[68]

■ REFERENCES

(1) Kojima, A.; Teshima, K.; Shirai, Y.; Miyasaka, T. Organometal Halide Perovskites as Visible-Light Sensitizers for Photovoltaic Cells. *J. Am. Chem. Soc.* **2009**, *131*, 6050−6051.

(2) Even, J.; Pedesseau, L.; Jancu, J.-M.; Katan, C. Importance of Spin-Orbit Coupling in Hybrid Organic-Inorganic Perovskites for Photovoltaic Applications. *J. Phys. Chem. Lett.* **2013**, *4*, 2999−3005.

(3) Lee, M. M.; Teuscher, J.; Miyasaka, T.; Murakami, T. N.; Snaith, H. J. Efficient Hybrid Solar Cells Based on Meso-Superstructured Organometal Halide Perovskites. *Science* **2012**, *338*, 643−647.

(4) Kim, H.-S.; Lee, C.-R.; Im, J.-H.; Lee, K.-B.; Moehl, T.; Marchioro, A.; Moon, S.-J.; Humphry-Baker, R.; Yum, J.-H.; Moser, J. E.; et al. Lead Iodide Perovskite Sensitized All-Solid-State Submicron Thin Film Mesoscopic Solar Cell with Efficiency Exceeding 9%. *Sci. Rep.* **2012**, *2*, 591.

(5) Baikie, T.; Fang, Y.; Kadro, J. M.; Schreyer, M.; Wei, F.; Mhaisalkar, S. G.; Graetzel, M.; White, T. J. Synthesis and Crystal Chemistry of the Hybrid Perovskite $CH_3NH_3PbI_3$ for Solid-State Sensitised Solar Cell Applications. *J. Mater. Chem. A* **2013**, *1*, 5628−5641.

(6) Brivio, F.; Walker, A. B.; Walsh, A. Structural and Electronic Properties of Hybrid Perovskites for High-Efficiency Thin-Film Photovoltaics from First-Principles. *APL Mater.* **2013**, *1*, 042111.

(7) Wehrenfennig, C.; Liu, M.; Snaith, H. J.; Johnston, M. B.; Herz, L. M. Homogeneous Emission Line Broadening in the Organo Lead Halide Perovskite $CH_3NH_3PbI_{3-x}Cl_x$. *J. Phys. Chem. Lett.* **2014**, *5*, 1300−1306.

(8) Snaith, H. J. Perovskites: The Emergence of a New Era for Low-Cost, High-Efficiency Solar Cells. *J. Phys. Chem. Lett.* **2013**, *4*, 3623−3630.

(9) Huang, L.-Y.; Lambrecht, W. R. L. Lattice Dynamics in Perovskite Halides $CsSnX_3$ with X = I, Br, Cl. *Phys. Rev. B: Condens. Matter Mater. Phys.* **2014**, *90*, 195201.

(10) Umari, P.; Mosconi, E.; De Angelis, F. Relativistic GW Calculations on $CH_3NH_3PbI_3$ and $CH_3NH_3SnI_3$ Perovskites for Solar Cell Applications. *Sci. Rep.* **2015**, *4*, 4467.

(11) Lin, Q.; Armin, A.; Nagiri, R. C. R.; Burn, P. L.; Meredith, P. Electro-optics of Perovskite Solar Cells. *Nat. Photonics* **2015**, *9*, 106−112.

(12) Zhang, W.; Eperon, G. E.; Snaith, H. J. Metal Halide Perovskites for Energy Applications. *Nat. Energy.* **2016**, *1*, 16048.

(13) Grätzel, M. The Light and Shade of Perovskite Solar Cells. *Nat. Mater.* **2014**, *13*, 838−842.

(14) Herz, L. M. Charge-Carrier Dynamics in Organic-Inorganic Metal Halide Perovskites. *Annu. Rev. Phys. Chem.* **2016**, *67*, 65−89.

(15) Miyata, A.; Mitioglu, A.; Plochocka, P.; Portugall, O.; Wang, J. T.-W.; Stranks, S. D.; Snaith, H. J.; Nicholas, R. J. Direct Measurement of the Exciton Binding Energy and Effective Masses for Charge Carriers in Organic-inorganic Tri-halide Perovskites. *Nat. Phys.* **2015**, *11*, 582−587.

(16) Wehrenfennig, C.; Eperon, G. E.; Johnston, M. B.; Snaith, H. J.; Herz, L. M. High Charge Carrier Mobilities and Lifetimes in Organolead Trihalide Perovskites. *Adv. Mater.* **2014**, *26*, 1584.

(17) Stoumpos, C. C.; Malliakas, C. D.; Kanatzidis, M. G. Semiconducting Tin and Lead Iodide Perovskites with Organic Cations: Phase Transitions, High Mobilities, and Near-Infrared Photoluminescent Properties. *Inorg. Chem.* **2013**, *52*, 9019−9038.

(18) Green, M.; Ho-Baillie, A.; Snaith, H. J. The Emergence of Perovskite Solar Cells. *Nat. Photonics* **2014**, *8*, 506.

(19) Wright, A. D.; Verdi, C.; Milot, R. L.; Eperon, G. E.; Pérez-Osorio, M. A.; Snaith, H. J.; Giustino, F.; Johnston, M. B.; Herz, L. M. Electron-phonon Coupling in Hybrid Lead Halide Perovskites. *Nat. Commun.* **2016**, *7*, 11755.

(20) Filippetti, A.; Mattoni, A.; Caddeo, C.; Saba, M. I.; Delugas, P. Low Electron-polar Optical Phonon Scattering as a Fundamental Aspect of Carrier Mobility in Methylammonium Lead Halide $CH_3NH_3PbI_3$ Perovskites. *Phys. Chem. Chem. Phys.* **2016**, *18*, 15352−15362.

(21) Bokdam, M.; Sander, T.; Stroppa, A.; Picozzi, S.; Sarma, D. D.; Franchini, C.; Kresse, G. Role of Polar Phonons in the Photo Excited State of Metal Halide Perovskites. *Sci. Rep.* **2016**, *6*, 28618.

(22) Létoublon, A.; Paofai, S.; Rufflé, B.; Bourges, P.; Hehlen, B.; Michel, T.; Ecolivet, C.; Durand, O.; Cordier, S.; Katan, C.; et al. Elastic Constants, Optical Phonons, and Molecular Relaxations in the High Temperature Plastic Phase of the $CH_3NH_3PbBr_3$ Hybrid Perovskite. *J. Phys. Chem. Lett.* **2016**, *7*, 3776−3784.

(23) Mattoni, A.; Filippetti, A.; Saba, M.; Caddeo, C.; Delugas, P. Temperature Evolution of Methylammonium Trihalide Vibrations at the Atomic Scale. *J. Phys. Chem. Lett.* **2016**, *7*, 529−535.

(24) Pérez-Osorio, M. A.; Milot, R. L.; Filip, M. R.; Patel, J. B.; Herz, L. M.; Johnston, M. B.; Giustino, F. Vibrational Properties of the Organic-Inorganic Halide Perovskite $CH_3NH_3PbI_3$ from Theory and Experiment: Factor Group Analysis, First-Principles Calculations, and Low-Temperature Infrared Spectra. *J. Phys. Chem. C* **2015**, *119*, 25703−25718.

(25) Brivio, F.; Frost, J. M.; Skelton, J. M.; Jackson, A. J.; Weber, O. J.; Weller, M. T.; Goñi, A. R.; Leguy, A. M. A.; Barnes, P. R. F.; Walsh, A. Lattice Dynamics and Vibrational Spectra of the Orthorhombic, Tetragonal, and Cubic Phases of Methylammonium Lead Iodide. *Phys. Rev. B: Condens. Matter Mater. Phys.* **2015**, *92*, 144308.

(26) Onoda-Yamamuro, N.; Matsuo, T.; Suga, H. Calorimetric and IR Spectroscopic Studies of Phase Transitions in Methylammonium Trihalogenoplumbates (II). *J. Phys. Chem. Solids* **1990**, *51*, 1383−1395.

(27) Glaser, T.; Müller, C.; Sendner, M.; Krekeler, C.; Semonin, O. E.; Hull, T. D.; Yaffe, O.; Owen, J. S.; Kowalsky, W.; Pucci, A.; et al. Infrared Spectroscopic Study of Vibrational Modes in Methylammonium Lead Halide Perovskites. *J. Phys. Chem. Lett.* **2015**, *6*, 2913−2918.

(28) Sendner, M.; Nayak, P. K.; Egger, D. A.; Beck, S.; Müller, C.; Epding, B.; Kowalsky, W.; Kronik, L.; Snaith, H. J.; Pucci, A.; et al. Optical Phonons in Methylammonium Lead Halide Perovskites and Implications for Charge Transport. *Mater. Horiz.* **2016**, *3*, 613−620.

(29) Ledinský, M.; Löper, P.; Niesen, B.; Holovský, J.; Moon, S.-J.; Yum, J.-H.; De Wolf, S.; Fejfar, A.; Ballif, C. Raman Spectroscopy of Organic-Inorganic Halide Perovskites. *J. Phys. Chem. Lett.* **2015**, *6*, 401−406.

(30) Zhou, Y.; Garces, H. F.; Padture, N. P. Challenges in the Ambient Raman Spectroscopy Characterization of Methylammonium Lead Triiodide Perovskite Thin Films. *Front. Optoelectron.* **2016**, *9*, 81−86.

(31) Gottesman, R.; Gouda, L.; Kalanoor, B. S.; Haltzi, E.; Tirosh, S.; Rosh-Hodesh, E.; Tischler, Y.; Zaban, A.; Quarti, C.; Mosconi, E.; et al. Photoinduced Reversible Structural Transformations in Free-Standing $CH_3NH_3PbI_3$ Perovskite Films. *J. Phys. Chem. Lett.* **2015**, *6*, 2332−2338.

(32) Grancini, G.; Marras, S.; Prato, M.; Giannini, C.; Quarti, C.; De Angelis, F.; De Bastiani, M.; Eperon, G. E.; Snaith, H. J.; Manna, L.; et al. The Impact of the Crystallization Processes on the Structural and Optical Properties of Hybrid Perovskite Films for Photovoltaics. *J. Phys. Chem. Lett.* **2014**, *5*, 3836−3842.

(33) Quarti, C.; Grancini, G.; Mosconi, E.; Bruno, P.; Ball, J. M.; Lee, M. M.; Snaith, H. J.; Petrozza, A.; De Angelis, F. The Raman Spectrum of the $CH_3NH_3PbI_3$ Hybrid Perovskite: Interplay of Theory and Experiment. *J. Phys. Chem. Lett.* **2014**, *5*, 279−284.

(34) Park, B.-W.; Jain, S. M.; Zhang, X.; Hagfeldt, A.; Boschloo, G.; Edvinsson, T. Resonance Raman and Excitation Energy Dependent Charge Transfer Mechanism in Halide-Substituted Hybrid Perovskite Solar Cells. *ACS Nano* **2015**, *9*, 2088−2101.

(35) Grimme, S. Semiempirical GGA-type Density Functional Constructed with a Long-range Dispersion Correction. *J. Comput. Chem.* **2006**, *27*, 1787−1799.

(36) Whalley, L. D.; Skelton, J. M.; Frost, J. M.; Walsh, A. Phonon Anharmonicity, Lifetimes and Thermal Transport in $CH_3NH_3PbI_3$ from Many-body Perturbation Theory. *Phys. Rev. B: Condens. Matter Mater. Phys.* **2016**, *94*, 220301.

(37) Barone, V.; Casarin, M.; Forrer, D.; Pavone, M.; Sambi, M.; Vittadini, A. Role and Effective Treatment of Dispersive Forces in Materials: Polyethylene and Graphite Crystals as Test Cases. *J. Comput. Chem.* **2009**, *30*, 934−939.

(38) Grimme, S.; Ehrlich, S.; Goerigk, L. Effect of the Damping Function in Dispersion Corrected Density Functional Theory. *J. Comput. Chem.* **2011**, *32*, 1456−1465.

(39) Tkatchenko, A.; Scheffler, M. Accurate Molecular Van Der Waals Interactions from Ground-State Electron Density and Free-Atom Reference Data. *Phys. Rev. Lett.* **2009**, *102*, 073005.

(40) Kolb, B.; Thonhauser, T. Van Der Waals Density Functional Study of Energetic, Structural, and Vibrational Properties of Small Water Clusters and Ice I_h. *Phys. Rev. B: Condens. Matter Mater. Phys.* **2011**, *84*, 045116.

(41) Giannozzi, P.; Baroni, S.; Bonini, N.; Calandra, M.; Car, R.; Cavazzoni, C.; Ceresoli, D.; Chiarotti, G. L.; Cococcioni, M.; Dabo, I.; et al. QUANTUM ESPRESSO: a Modular and Open-Source Software

Project for Quantum Simulations of Materials. *J. Phys.: Condens. Matter* **2009**, *21*, 395502.

(42) Gonze, X.; Amadon, B.; Anglade, P.-M.; Beuken, J.-M.; Bottin, F.; Boulanger, P.; Bruneval, F.; Caliste, D.; Caracas, R.; Coté, M.; et al. ABINIT: First-principles Approach to Material and Nanosystem Properties. *Comput. Phys. Commun.* **2009**, *180*, 2582−2615.

(43) Gonze, X.; Beuken, J.-M.; Caracas, R.; Detraux, F.; Fuchs, M.; Rignanese, G.-M.; Sindic, L.; Verstraete, M.; Zerah, G.; Jollet, F.; et al. First-principles Computation of Material Properties: the {ABINIT} Software Project. *Comput. Mater. Sci.* **2002**, *25*, 478−492.

(44) Weller, M. T.; Weber, O. J.; Henry, P. F.; Di Pumpo, A. M.; Hansen, T. C. Complete Structure and Cation Orientation in the Perovskite Photovoltaic Methylammonium Lead Iodide between 100 and 352 K. *Chem. Commun.* **2015**, *51*, 4180−4183.

(45) Whitfield, P. S.; Herron, N.; Guise, W. E.; Page, K.; Cheng, Y. Q.; Milas, I.; Crawford, M. K. Structures, Phase Transitions and Tricritical Behavior of the Hybrid Perovskite Methyl Ammonium Lead Iodide. *Sci. Rep.* **2016**, *6*, 35685.

(46) Perdew, J. P.; Burke, K.; Ernzerhof, M. Generalized Gradient Approximation Made Simple. *Phys. Rev. Lett.* **1996**, *77*, 3865−3868.

(47) Ceperley, D. M.; Alder, B. J. Ground State of the Electron Gas by a Stochastic Method. *Phys. Rev. Lett.* **1980**, *45*, 566−569.

(48) Vanderbilt, D. Soft Self-consistent Pseudopotentials in a Generalized Eigenvalue Formalism. *Phys. Rev. B: Condens. Matter Mater. Phys.* **1990**, *41*, 7892−7895.

(49) Troullier, N.; Martins, J. L. Efficient Pseudopotentials for Plane-Wave Calculations. *Phys. Rev. B: Condens. Matter Mater. Phys.* **1991**, *43*, 1993−2006.

(50) Hamann, D. R. Optimized Norm-Conserving Vanderbilt Pseudopotentials. *Phys. Rev. B: Condens. Matter Mater. Phys.* **2013**, *88*, 085117.

(51) Becke, A. D.; Johnson, E. R. A Density-functional Model of the Dispersion Interaction. *J. Chem. Phys.* **2005**, *123*, 154101.

(52) Johnson, E. R.; Becke, A. D. A Post-Hartree-Fock Model of Intermolecular Interactions: Inclusion of Higher-order Corrections. *J. Chem. Phys.* **2006**, *124*, 174104.

(53) Giustino, F. *Materials Modelling Using Density Functional Theory: Properties and Predictions*; Oxford University Press, 2014.

(54) Martin, R. M. *Electronic Structure: Basic Theory and Practical Methods*; Cambridge University Press, Cambridge, U.K., 2010.

(55) Du, M. H. Efficient Carrier Transport in Halide Perovskites: Theoretical Perspectives. *J. Mater. Chem. A* **2014**, *2*, 9091−9098.

(56) Hirasawa, M.; Ishihara, T.; Goto, T.; Uchida, K.; Miura, N. Magnetoabsorption of the Lowest Exciton in Perovskite-type Compound $(CH_3NH_3)PbI_3$. *Phys. B* **1994**, *201*, 427−430.

(57) Poglitsch, A.; Weber, D. Dynamic Disorder in Methylammoniumtrihalogenoplumbates (II) Observed by Millimeter-Wave Spectroscopy. *J. Chem. Phys.* **1987**, *87*, 6373−6378.

(58) Marom, N.; DiStasio, R. A.; Atalla, V.; Levchenko, S.; Reilly, A. M.; Chelikowsky, J. R.; Leiserowitz, L.; Tkatchenko, A. Many-Body Dispersion Interactions in Molecular Crystal Polymorphism. *Angew. Chem., Int. Ed.* **2013**, *52*, 6629−6632.

(59) Reilly, A. M.; Tkatchenko, A. *van der Waals Dispersion Interactions in Molecular Materials: Beyond Pairwise Additivity* **2015**, *6*, 3289−3301.

(60) Kronik, L.; Tkatchenko, A. Understanding Molecular Crystals with Dispersion-Inclusive Density Functional Theory: Pairwise Corrections and Beyond. *Acc. Chem. Res.* **2014**, *47*, 3208−3216.

(61) Papavassiliou, G. C.; Koutselas, I. B. Structural, Optical and Related Properties of Some Natural Three- and Lower-dimensional Semiconductor Systems. *Synth. Met.* **1995**, *71*, 1713−1714.

(62) Filip, M. R.; Giustino, F. GW Quasiparticle Band Gap of the Hybrid Organic-Inorganic Perovskite $CH_3NH_3PbI_3$: Effect of Spin-Orbit Interaction, Semicore Electrons, and Self-Consistency. *Phys. Rev. B: Condens. Matter Mater. Phys.* **2014**, *90*, 245145.

(63) Mattoni, A.; Filippetti, A.; Caddeo, C. Modeling Hybrid Perovskites by Molecular Dynamics. *J. Phys.: Condens. Matter* **2017**, *29*, 043001.

(64) Mattoni, A.; Filippetti, A.; Saba, M. I.; Delugas, P. Methylammonium Rotational Dynamics in Lead Halide Perovskite by Classical Molecular Dynamics: The Role of Temperature. *J. Phys. Chem. C* **2015**, *119*, 17421−17428.

(65) Li, B.; Kawakita, Y.; Liu, Y.; Wang, M.; Matsuura, M.; Shibata, K.; Ohira-Kawamura, S.; Yamada, T.; Lin, S.; Nakajima, K.; et al. Polar Rotor Scattering as Atomic-level Origin of Low Mobility and Thermal Conductivity of Perovskite $CH_3NH_3PbI_3$. *Nat. Commun.* **2017**, *8*, 16086.

(66) Chen, T.; Foley, B. J.; Ipek, B.; Tyagi, M.; Copley, J. R. D.; Brown, C. M.; Choi, J. J.; Lee, S.-H. Rotational Dynamics of Organic Cations in the $CH_3NH_3PbI_3$ perovskite. *Phys. Chem. Chem. Phys.* **2015**, *17*, 31278−31286.

(67) Druzbicki, K.; Pinna, R. S.; Rudic, S.; Jura, M.; Gorini, G.; Fernandez-Alonso, F. Unexpected Cation Dynamics in the Low-Temperature Phase of Methylammonium Lead Iodide: The Need for Improved Models. *J. Phys. Chem. Lett.* **2016**, *7*, 4701−4709.

(68) Momma, K.; Izumi, F. *VESTA*: a Three-Dimensional Visualization System for Electronic and Structural Analysis. *J. Appl. Crystallogr.* **2008**, *41*, 653−658.